Materials and Design 155 (2018) 375–383

Contents lists available at ScienceDirect

Materials and Design

journal homepage: www.elsevier.com/locate/matdes

Liquid metal embrittlement in laser beam welding of Zn-coated 22MnB5 steel

M.H. Razmpoosh [a,*], A. Macwan [b], E. Biro [a], D.L. Chen [c], Y. Peng [d], F. Goodwin [e], Y. Zhou [a]

[a] Centre for Advanced Materials Joining, Department of Mechanical & Mechatronics Engineering, University of Waterloo, 200 University Avenue West, Waterloo N2L 3G1, Ontario, Canada
[b] ArcelorMittal Global Research, 1390 Burlington Street east, Hamilton L8N 3J5, Ontario, Canada
[c] Department of Mechanical and Industrial Engineering, Ryerson University, 350 Victoria Street, Toronto M5B 2K3, Ontario, Canada
[d] Central Iron & Steel Research Institute (CISRI), Beijing 100081, China
[e] International Zinc Association, Durham, NC 27713, USA

HIGHLIGHTS

- This work presents liquid metal embrittlement (LME) during externally loaded fiber laser welding of Zn-coated 22MnB5 steel.
- The results confirmed a direct relation between the external load and LME susceptibility.
- The threshold tensile stress of about 80% YS is needed to trigger the embrittlement.
- Zn penetrates along prior austenite high-angle grain boundaries within upper-critical heat affected zone.
- α-Fe(Zn) transformation along the LME-crack assists the loss of ductility.

GRAPHICAL ABSTRACT

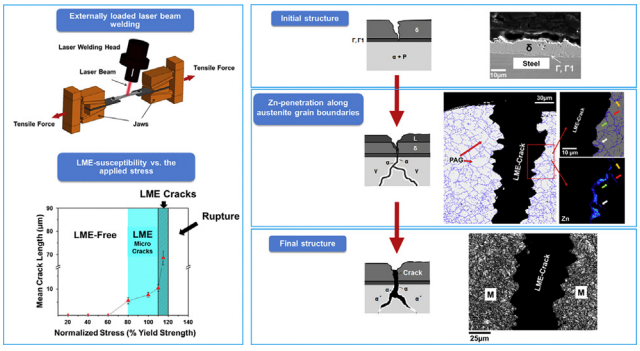

ARTICLE INFO

Article history:
Received 16 February 2018
Received in revised form 25 May 2018
Accepted 29 May 2018
Available online 30 May 2018

Keywords:
Liquid metal embrittlement
Laser beam welding
Press-hardening steel
Microstructure
Zn

ABSTRACT

Despite frequent reports of liquid metal embrittlement (LME) during resistance spot welding, no work has been done to investigate the LME sensitivity in laser beam welding (LBW) of advanced high strength steels. The present study was therefore undertaken to reflect the LME sensitivity of Zn-coated 22MnB5 press-hardening steel as a function of stress intensity and heat input during LBW. The results proved a direct relation between the external load and LME susceptibility, where the threshold tensile stress of about 80%YS is necessary to trigger the embrittlement. Electron backscatter diffraction (EBSD) in conjunction with electron probe micro-analyzer (EPMA) results confirmed the intergranular penetration of Zn along the prior austenite high-angle grain boundaries in upper-critical heat affected zone (UCHAZ). The presence of Zn over the maximum Zn-solubility of austenite promotes α-Fe(Zn) transformation along the LME-crack which assists the loss of ductility. The present findings provide an understanding of the mechanism of embrittlement in UCHAZ and suggest solutions to mitigate the LME in LBW of boron steels.

1. Introduction

Liquid metal embrittlement (LME) is catastrophic failure of a ductile material, by rapid penetration of a wetting liquid metal (Zn, Ga, Bi and etc.) along the grain boundary network in the presence of internal

* Corresponding author.
E-mail address: mhrazmpoosh@uwaterloo.ca (M.H. Razmpoosh).

https://doi.org/10.1016/j.matdes.2018.05.065
0264-1275/

(residual) or external stresses [1–3]. LME is widely reported in the literature in various high-temperature processes such as galvanizing, hot-press forming and welding of Zn-coated steel sheets [4–9]. LME during resistance spot welding (RSW) is a known concern for various Zn-coated advanced high strength steels (AHSS). High alloy-content, unavoidable presence of liquid Zn on the surface and tensile stresses during welding leads to susceptibility to LME during RSW of AHSS such as twinning induced plasticity (TWIP) steels [5,6]. As Ashiri et al. [5] claimed, LME could considerably affect the weldable current range in RSW of TWIP steel. However, LME during laser beam welding (LBW) has only briefly been reported and the underlying mechanism is still ambiguous. In this regard, Favez et al. [7] reported the liquid metal penetration into the austenite grain boundaries in regions adjacent to the weld line during LBW of stainless steel.

It is believed that the overall LME crack path is governed by the stress state. However, several studies [7–11] also claimed that the local propagation path of the LME crack is governed by the grain boundary characteristics [7,10]. The thermodynamic driving force (F_D) for liquid metal penetration is helping to elucidate the role of grain boundaries in the embrittlement phenomenon:

$$F_D = \gamma_{GB} - 2\gamma_{S/L} \quad (1)$$

where γ_{GB} is the grain boundary energy and $\gamma_{S/L}$ is the solid/liquid interface energy [10]. In this regard, the liquid metal penetration into the grain boundaries becomes energetically favorable where a large-misorientation grain boundary is replaced with an iron-saturated liquid film ($2\gamma_{S/L} < \gamma_{GB}$). In fact, higher γ_{GB} results in an increased driving force for the penetration [1,7,10]. The Al-Ga system is the most widely studied to provide the fundamental perspective of the relationship between the LME susceptibility and the grain boundary characteristics [1,2,8–12]. In situ TEM study by Hugo et al. [8] demonstrated that the grain boundaries with misorientation angles (θ) lower than 15° showed a slow penetration rate. Generally, most of the high penetration rate grain boundaries possess the grain boundary energy over 0.6 J/m^2, where the threshold energy value for the penetration is governed by $\gamma_{S/L}$ value.

Based on the experimental [8–10] and simulation [1,11] research works, it has been revealed that in addition to the intrinsic material properties e.g. grain boundary/interfacial energy interplay, grain boundary diffusivity, and solubility, the LME tendency is also governed by the external variables such as composition of the liquid, temperature, and the applied stress. Specifically, it is reported that the penetration of liquid layer into the grain boundaries is highly dependent on the applied stress [7,9,11]. According to Nam et al. [11], it is confirmed that liquid Ga penetrates into the Al grain boundaries much faster by increasing the applied uniaxial tensile stress. More importantly, it is evidenced that the effect of the applied stress on the Ga penetration depth at the early stage of liquid groove formation is not significant [11]. However, over a stress threshold, tensile stress substantially accelerates grain boundary penetration. This critical stress is attributed to the formation of dislocations along the grain boundaries over the threshold stress [11]. Temperature, as the other main external variable, is believed to substantially affect the LME phenomenon [11,13]. Simulation results [11] confirmed that the increase in temperature accelerates nucleation of dislocations along the grain boundaries and overall penetration of the liquid metal.

So far, various methods have been proposed to mitigate LME in steel alloys. The results by Beal et al. [14,15] confirmed that embrittlement only occurs in a limited temperature range (700–950 °C) called "ductility trough". Hence, by avoiding the risk temperature range during the processing, the LME-cracking could highly be prevented. In addition, higher holding times by the formation of Fe,Mn,Zn stable intermetallic compounds at the Zinc penetration zone can effectively suppress LME during monotonic tension. However, from a practical point of view temperature range of 700–950 °C and low exposure times could easily come across during welding. As Ashiri et al. [6] claimed, the sensitivity of Zn-LME is highly relying on Zn-coating type where Electrogalvanized (EG) coatings highly suppress LME-cracking during welding. In addition, an innovative way to obtain LME-free joints by impulse RSW is proposed which is able to extend the weldable current range by 85% [5]. In addition, cyclic loading of ferritic–martensitic steels in the presence of aggressive liquid metal ends in high crack growth rates [16,17]. Nevertheless, by the presence of an adequate amount of oxygen in the liquid metal, the material can grow a protective oxide scale [16].

In the recent years, the production of ultra-high strength components with tailored properties by press hardening of boron steels gained a growing attention for several potential applications such as: A-pillars, B-pillars, bumpers, roof rails, rocker rails, and tunnels [18–24]. Due to issues regarding the Al-Si-coating mixing into the FZ and formation of a continuous structure of δ-ferrite, Zn-coating arose as an alternative for the conventional Al-Si-coating for preventing oxidation and decarburization during press-hardening of boron steels [25]. In this regard, recently Kang et al. [26] clearly confirmed the susceptibility of Zn-coated PHS to the intergranular embrittlement through Gleeble high-temperature tensile testing. As claimed by these authors, a premature failure occurred in Zn-coated PHS at 850 °C due to LME and ductility level decreased from 35% (uncoated condition) to 9%. In addition, Lee et al. [27] reported the occurrence of LME during austenitization/die-quenching of Zn-coated 22MnB5 steel in the outer wall of the press-hardened component. These results demonstrate that Zn-coated PHS has a potential for Zn-LME when subjected to high-temperature processes under applied tensile stresses, such as laser welding. Hence, the present work addresses the influence of process and material parameters on LME phenomenon during LBW of Zn-coated 22MnB5 PHS. The present findings also provide a new insight on LME during the production of tailor welded blanks (TWBs) of Zn-coated advanced high strength steels (AHSSs) in automotive structural components.

2. Material and experimental procedure

22MnB5 boron steel sheets with a nominal thickness of 1.2 mm were used in the present study. Table 1 shows the chemical composition of the experimental material. The Galvanneal (GA) coating was characterized in detail by means of electron probe micro analysis (EPMA) and X-Ray Diffraction (XRD). Fig. 1 represents the experimental setup for applying external loading during LBW. The machined tensile specimens were used for the welding trials (Fig. 2). Fig. 3 shows the engineering stress vs. strain curve of the material with yield strength of 410 MPa and ultimate tensile strength of 600 MPa. Externally loaded laser bead-on-plate trials were performed using an IPG Photonics ytterbium fiber laser system (YLS-6000-S2) mounted to a Panasonic robotic arm. The fiber core diameter, the spot size, and the beam focal length were 0.3, 0.6 and 200 mm, respectively. The experiments were carried out using a laser power range of 4–6 kW and a travel speed range of 8–20 m/min. It should be pointed out that in order to investigate the influence of applied tensile stress on LME susceptibility, the normalized tensile stress with respect to the yield strength of the experimental material has been taken into consideration. The direction of the applied tensile stresses was parallel to the direction of welding (Fig. 2) and the laser bead located at the center of the gauge length.

In order to investigate the microstructure, sections were cut from the welded material in a plane parallel to the weld line (3 mm far from the weld center-line). After mounting, a precise grinding (1200grit) was followed to reach LME-cracks. Afterwards, the prepared samples were polished to 0.25 μm and were investigated via scanning electron microscopy (SEM), equipped with energy-dispersive

Table 1
The chemical composition (wt%) of the 22MnB5 steel.

C	Mn	Si	P	S	Al	Cr	Ti	B	Fe
0.23	1.19	0.25	0.016	0.002	0.05	0.20	0.031	0.0030	Bal.

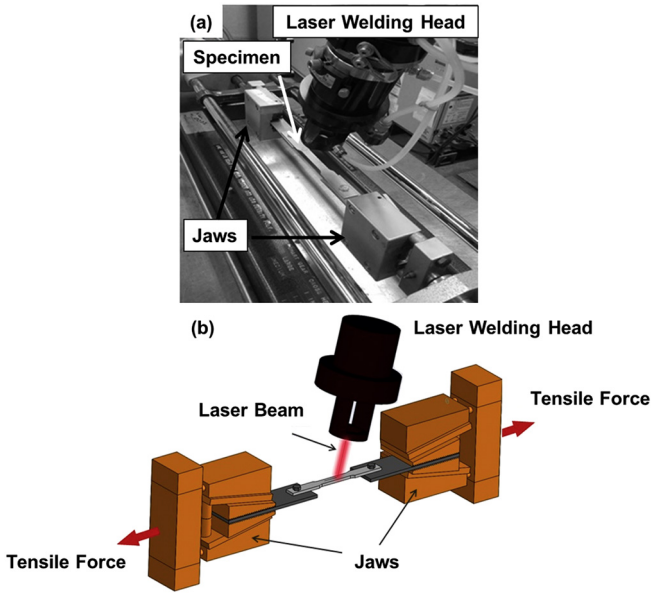

Fig. 1. (a) and (b) The developed setup to apply external loading during laser beam welding.

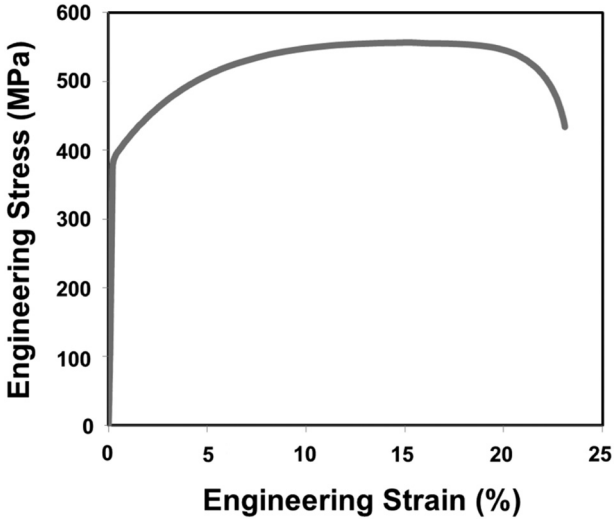

Fig. 3. Engineering stress-strain curve of the experimental 22MnB5 steel.

spectroscopy (EDS) and wavelength-dispersive spectroscopy (WDS) for elemental analysis. In detail analysis of the microstructure and the grain boundaries was carried out by means of electron backscatter diffraction (EBSD). The conventional fine polishing using a colloidal silica solution was followed for the EBSD sample preparation. High-resolution EBSD system attached to the JEOL JSM 7000f was used. The EBSD operating condition was 20 kV accelerating voltage and the step size of 0.25 μm. As conventional, low-angle boundaries (LABs) and high-angle boundaries (HABs) corresponds to the boundaries with misorientations of $0.7° < \theta < 15°$ and $\theta > 15°$, respectively.

Various approaches could be used to determine the LME susceptibility: total length of cracks or an overall number of cracks as well as the maximum crack length [28]. As reported by Ashiri et al. [5], the longest cracks could propagate easier under the action of applied stresses because less energy is required. Therefore, the average length of the longest observed micro-cracks has been taken into consideration in the present study. In the present study, the term of "micro-crack" refers to LME-cracks with a length below 10 μm. Any longer crack is referred as "LME crack". It should be noted that according to GM4485M specification for laser welds [29], the joint shall be free of any crack size.

3. Results and discussion

Fig. 4a shows the initial microstructure of the as-received material with a ferritic matrix and dispersed colonies of pearlite structure. This is in agreement with the engineering stress vs. strain curve of the material (Fig. 4). Moreover, Fig. 4b–d presents the SEM cross-section view of the Zn-coating. The micrograph and EPMA elemental distribution map results illustrate the presence of two main layers inside the coating. In order to provide identification of the phases, XRD analysis was carried out and the results confirmed that the coating mainly consisted of Γ-Fe_3Zn_{10}, Γ1-Fe_5Zn_{21} and δ-$FeZn_{10}$ phases (Fig. 4e). Therefore, the uppermost layer (~7 μm in thickness) has been identified as δ-phase and Γ/Γ1-phases were located in the steel-coating interface (~1–2 μm in thickness). The presence of Γ/Γ1 and δ phases in the coating is in accordance with previous research works, where the (Γ/Γ1) and δ phases are holding about 75 and 90 wt% of Zn, respectively [30].

It has been observed that laser welding under the applied external load results in the formation of several cracks in the upper-critical heat-affected zone (UCHAZ). Fig. 5 shows the influence of the applied external load on the mean LME-crack length, where the normalized tensile stress to the yield stress (YS) of the experimental material was used. Hereafter, the mean crack length is defined as an average of the maximum length of cracks observed within the UCHAZ in 3 identical trials. As seen in Fig. 5, LME micro-cracking in the experimental material is mainly in effect between 80 and 110% of YS. However, LME-free joints can be achieved if the applied tensile stress is <80% of YS. Fig. 6a presents the cross-sectional view of the UCHAZ, where LME micro-cracks appear. As seen, the micro-crack initiates from the coating-steel interface and subsequently propagates into the steel substrate. Energy-dispersive spectroscopy (EDS) analysis confirmed the presence of Zn in the vicinity of micro-crack, showing the role of penetrated Zn in weakening at early stages of micro-crack formation (Fig. 6b).

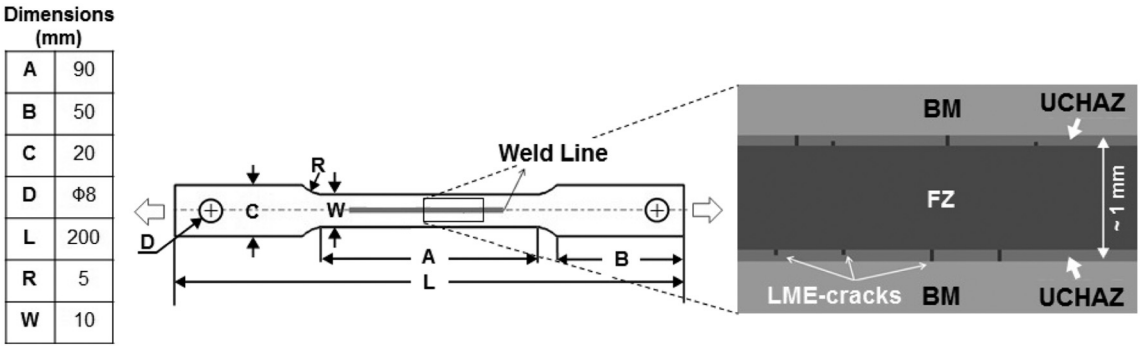

Fig. 2. Schematic illustration of the specimen, weld line configuration and the observed LME-cracks within the UCHAZ (weld line: 50 mm in length) (BM: Base material, FZ: Fusion zone, UCHAZ: Upper-critical heat-affected zone).

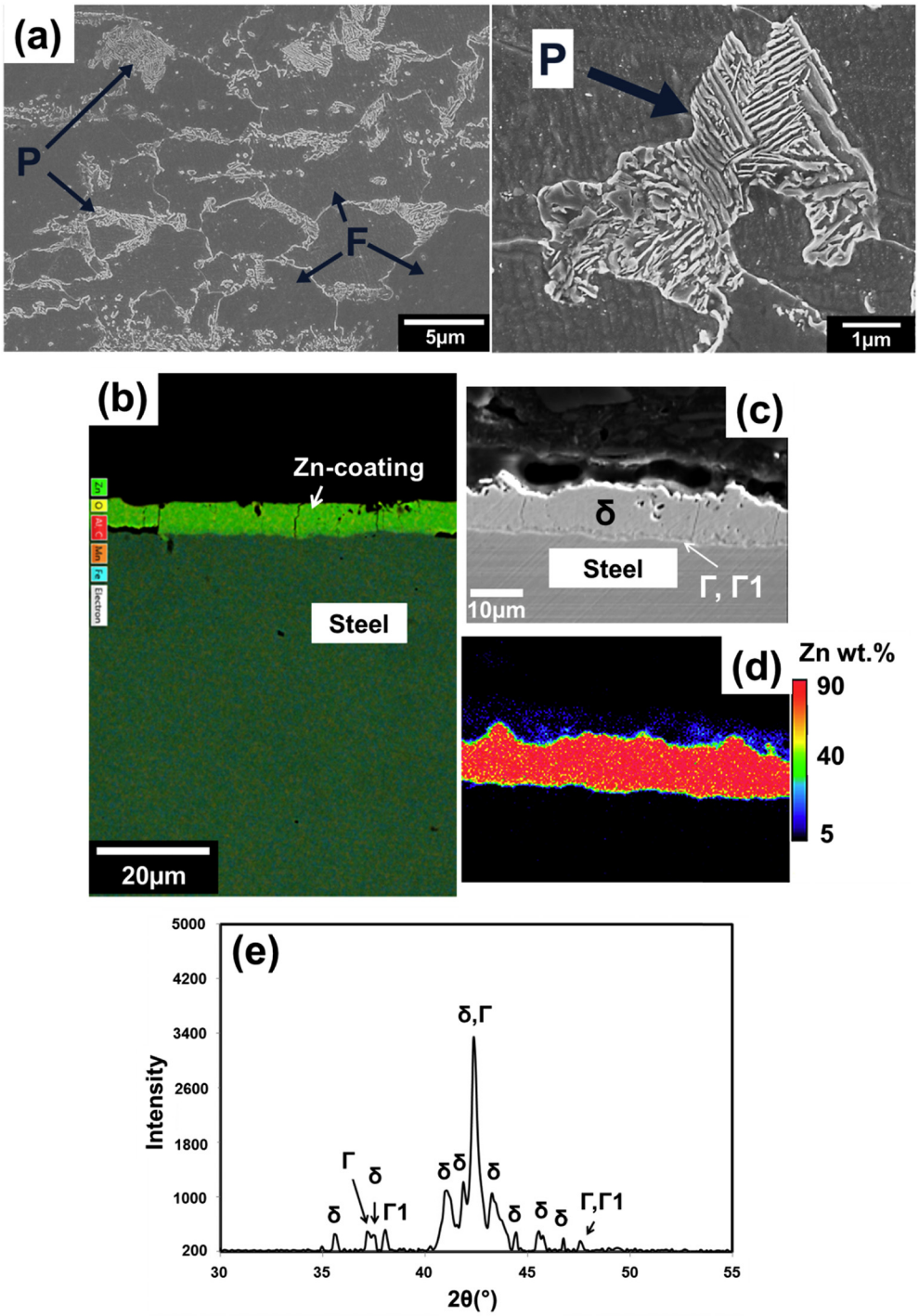

Fig. 4. (a) Representative microstructure of the as-received 22MnB5 steel, cross sectional (b) EDS elemental distribution map, (c) SEM micrograph, (d) EPMA Zn distribution map, and (e) XRD phase identification of the Zn-coating (where F: Ferrite, P: Pearlite).

It was observed that at 115% of YS, LME-cracks with an average length of about 70 μm appear in the UCHAZ (Fig. 7a). Ultimately, by exceeding 120% of YS an abrupt rupture during LBW takes place which is attributed to a rapid crack propagation into the FZ. Fig. 7b displays the propagation of LME-cracks from the UCHAZ into the FZ at tensile stresses over 120% of the YS. In other words, due to a low strength of the molten material in the FZ, any propagation of cracks into the FZ at high stresses would end in a sudden fracture. Micrograph taken from the fracture surface indicates the presence of 14.9 wt% of Zn (Fig. 7b). The observed behavior is in agreement with the LME-failure of Zn-coated 22MnB5 steel under high-temperature tensile testing at 850 °C [26].

Fig. 8 shows EBSD results around the LME-crack opening area in the UCHAZ. The EBSD phase map (bcc phase: red), as well as the orientation map, confirm the presence of a full martensitic structure with a lath martensite morphology in the vicinity of the LME-crack. The presence of negligible retained austenite in the martensitic structure is attributed to very high hardenability of the material as a consequence of the boron-addition and is in agreement with previous reports [31,32]. As discussed, the emerged austenite grains in the UCHAZ transforms to

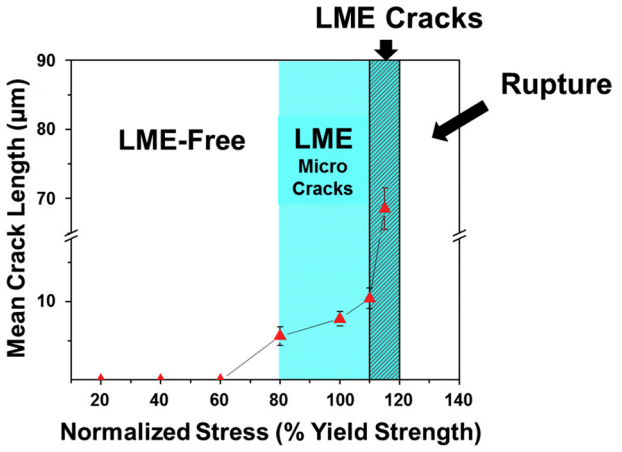

Fig. 5. Mean crack length vs. the applied tensile stress (under constant heat input per unit thickness of 20 J/mm^2).

martensite during the cooling cycle due to the high hardenability of 22MnB5 steel. To elucidate the role of austenite grain boundaries in penetration of Zn, prior austenite grains (PAGs) should be identified. Based on the literature, there exist two main methods for reconstruction of PAGs from EBSD data: complex reconstruction algorithm developed by Nyyssönen et al. [33] and the simpler method described by Hutchinson et al. [31]. The later method is mainly supported by the fact that in a typical martensitic structure boundaries resulted from shear transformation are either LABs or in the range of 50 to 63° [34]. As Ryde [34] suggested, PAGs in EBSD map could be identified by HABs excluding misorientations around Σ3 (60° [111]) relationship, as most of the boundaries resulted from martensitic transformation show Σ3 relationship. In contrast, packets of martensite are commonly having misorientation over 5° and in a similar manner, excluding martensitic transformation induced Σ3 relationship [34]. Based on the comparison by Jarvinen et al. [35], it is indicated that both methods reconstruct almost same PAG structures. Therefore, in this study PAG structure reconstructed from the EBSD data following the method used by Hutchinson et al. [31]. Fig. 9a represents the modified EBSD grain map near the LME-crack opening area, revealing prior austenite grain boundaries (PAGBs) (blue lines). The LME-crack propagated intergranularly along prior austenite HABs and it is most likely that the LME-crack did not follow the martensite packet boundaries. This indicates that the LME-crack only propagates before the transformation of martensite during the cooling cycle of the welding. Otherwise, due to the stress concentration at the tip of the crack after the formation of martensite, the LME-crack tends to follow inter-packets route as well. More in-detail EPMA Zn-distribution and EBSD maps in Fig. 9b and c also illustrate how Zn penetrated along PAGBs in side-branches of the main LME-crack. Same color arrows in Fig. 9b and c illustrate corresponding PAGBs and Zn-penetration.

It is noted that due to the limited solubility of Zn in austenite at 900 °C, Zn acts as ferrite stabilizer [27]. As claimed by Cho et al. [36], the formation of α-Fe(Zn) at regions surrounding the LME-crack assist the loss of ductility. Fig. 10a indicates a quantitative distribution of Zn at the LME-crack and side-branches. According to Fig. 10b, the Zn content in the crack is in the range of 5–42 wt%. As delineated by Kang et al. [26], the maximum solubility of Zn in austenite and ferrite at the UCHAZ temperature range (>850 °C) is about 7 and 40 wt%, respectively. Therefore, the presence of 42 wt% Zn in the vicinity of the LME-crack is in accordance with the solubility range of Zn in ferrite. In other words, as the local Zn content exceeds the maximum solubility in the austenite (7 wt%), α-Fe(Zn) becomes stable over the austenite. By the formation of α-Fe(Zn) around the PAGBs, Zn content could reach up to 45 wt%. Based on Fig. 10b, it is worth to mention that lower Zn content in the side-branch indicates the diffusion nature of Zn penetration along PAGBs.

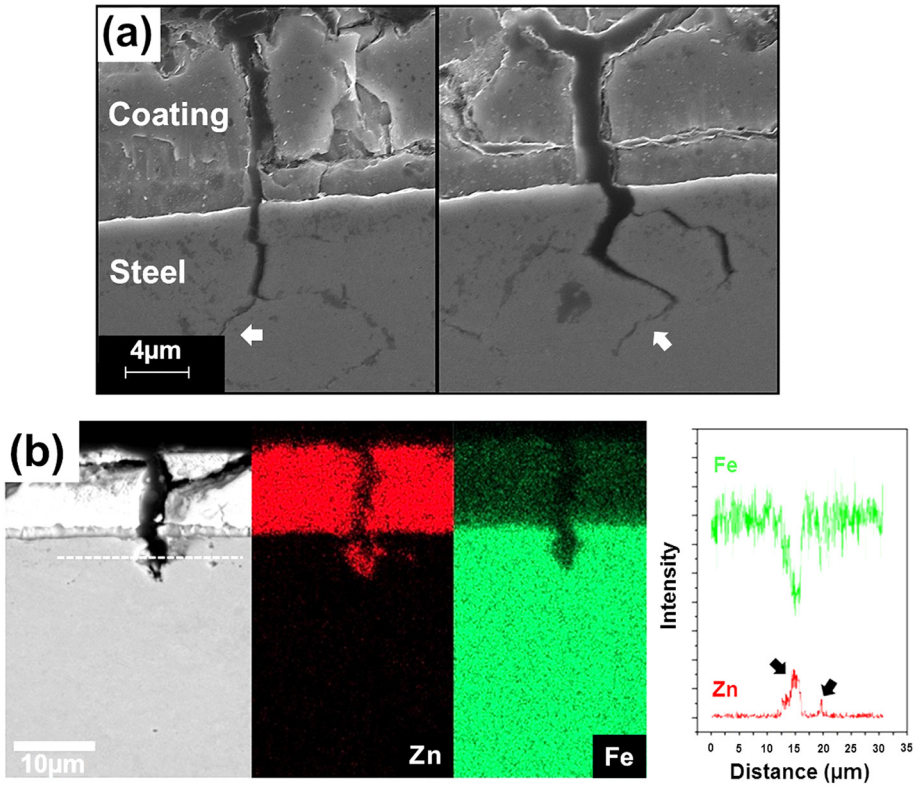

Fig. 6. (a) Representative LME micro-cracks formed in the UCHAZ under external loading (white arrows), and (b) the corresponding Zn and Fe element map of the LME micro-crack and Zn distribution along the dashed line.

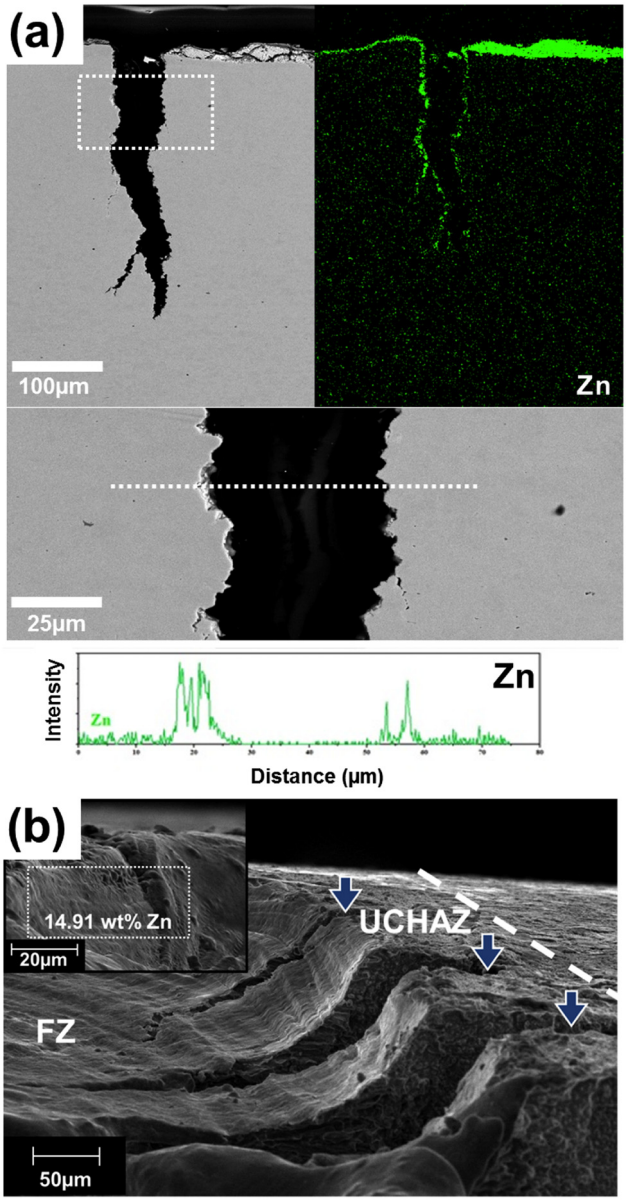

Fig. 7. (a) SEM micrograph and Zn distribution map of the LME-crack at 115% of the YS, and (b) propagation of LME-cracks formed within the UCHAZ to the FZ during abrupt rupture (arrows) and the presence of Zn on the fracture surface of the specimen.

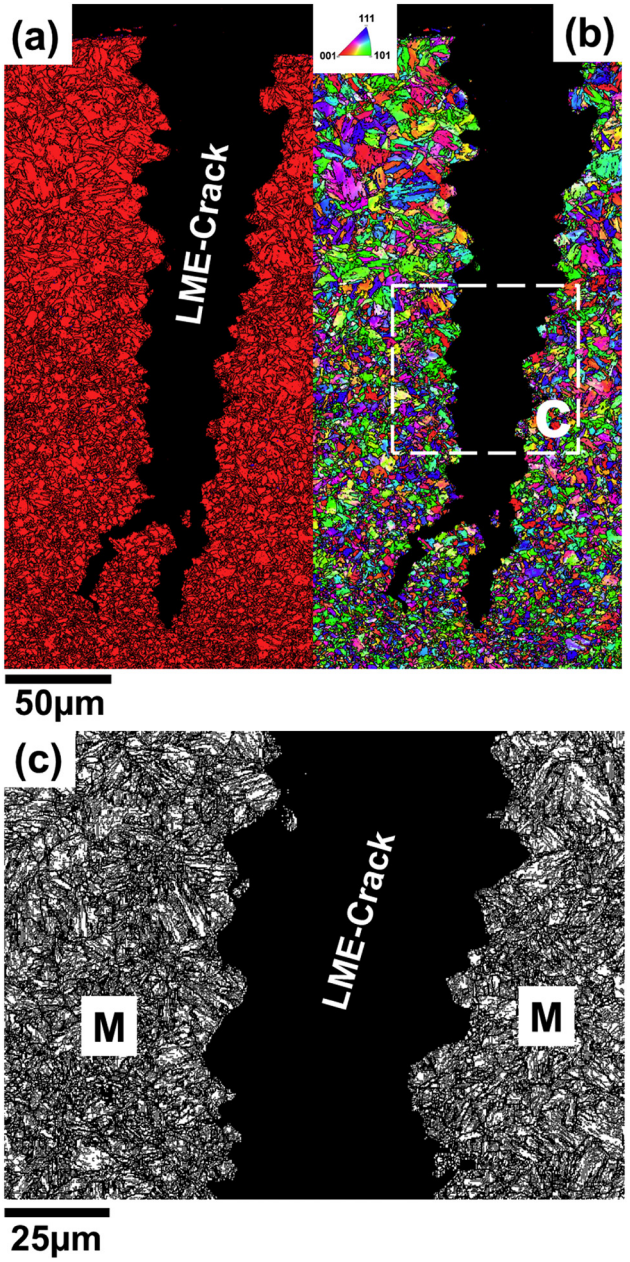

Fig. 8. The EBSD (a) phase map (red: bcc, blue: fcc), (b) orientation map around the LME-crack opening area, (c) the presence of the martensite lath structure around the LME-crack (M: Martensite).

So far, different approaches [34,37] have been proposed to discriminate ferrite and martensite as they possess close crystal structure and hence, similar appearance in EBSD phase map. Cho et al. [36] differentiated α-Fe(Zn) grains on either side of LME-crack based on the absence of lath martensite morphology. Other research works [34,37] also pointed out other approaches such as the threshold image quality, the band slope technique and the discrimination based on grain size distribution, and morphology. However, the morphology-based technique was used in the present work as the stable α-Fe(Zn) grains did not participate in martensitic transformation during the cooling cycle. Fig. 10c represents the EBSD orientation map in the vicinity of the LME-crack. As arrows indicate, the penetration of Zn along the austenite HABs at elevated temperatures promoted the formation of fine α-Fe(Zn) grains holding an orientation different from the martensitic matrix. It should be noted that only boundaries in the range of 15–50° have been revealed in Fig. 10c. This allows to differentiate nucleated fine α-Fe(Zn) grains (showing HABs) from the potential martensite packets or lathes.

To provide a thorough understanding of the underlying LME mechanism in LBW of GA-coated material, the schematic of multiple stages of the embrittlement is illustrated in Fig. 11. In this model, first, the δ and Γ/Γ1 phases within the coating partially melt over the UCHAZ during the heating cycle. As mentioned earlier, Γ/Γ1 and δ phases are holding about 75 and 90 wt% of Zn, respectively. According to the Fe-Zn binary phase diagram [38] and due to the different Zn-content, partial melting of Γ and δ phases starts at 782 and 665 °C, respectively. It is most likely that the partially melted Zn reaches the steel interface mainly by flowing through the pre-existing cracks in the brittle coating or the cracks created due to the applied tensile stresses (II). As the liquid-Zn reaches the substrate, it starts to penetrate by diffusion through the austenite grain boundaries (III). By penetration of Zn along the austenite HABs and under the effect of the applied tensile stress, material decohesion takes place and LME-cracks open. By rapid

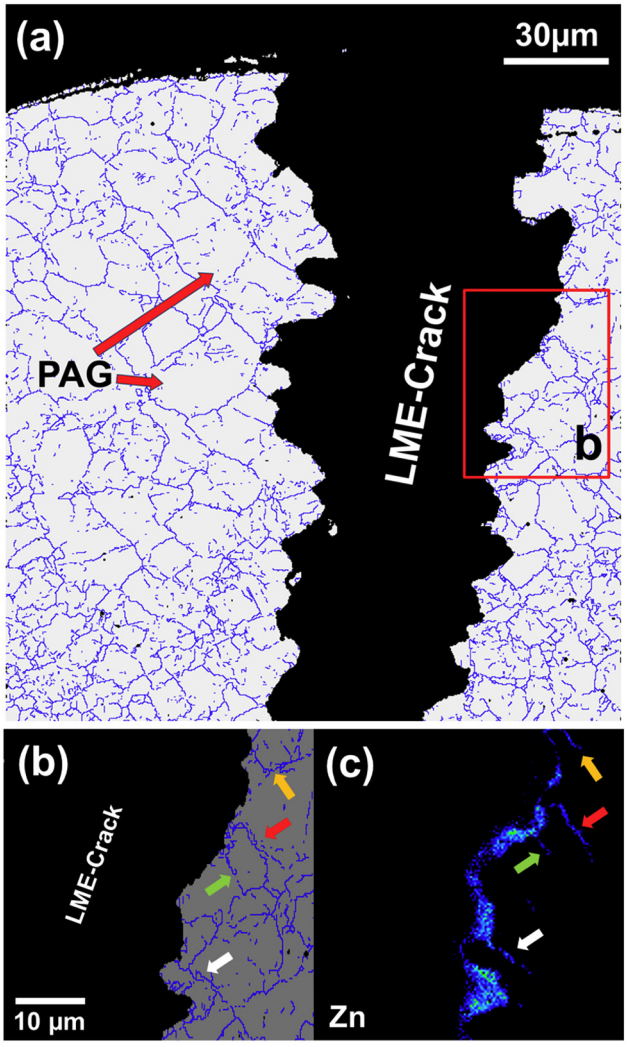

Fig. 9. (a) and (b) Prior austenite grains boundaries (blue lines) around the LME-crack opening area, and (c) corresponding EMPA Zn distribution map (same color arrows show the diffusion of Zn along the austenite high-angle boundaries) (PAG: Prior austenite grain).

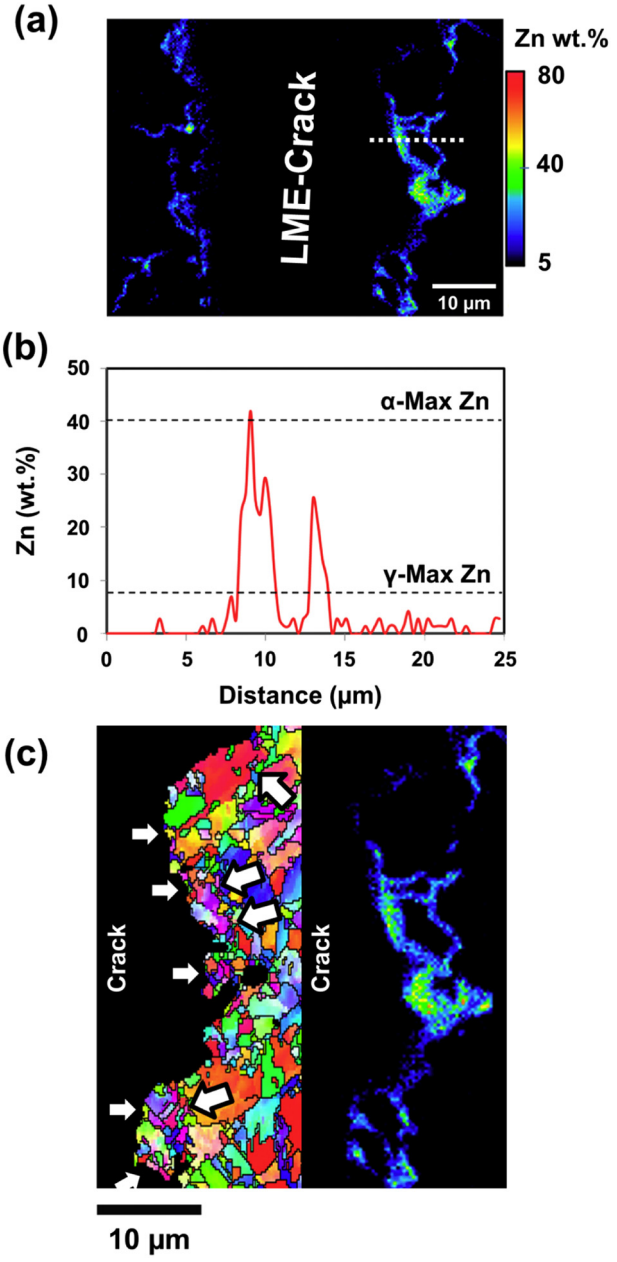

Fig. 10. (a) EPMA Zn distribution mapping in vicinity of the LME-crack, (b) corresponding EPMA line scan analysis over the white dashed line as well as the maximum solubility of Zn in γ and α, and (c) the formation of fine α-Fe(Zn) grains along the LME-crack opening (white arrows) (γ: Austenite, α: Ferrite).

crack opening, it is expected that more fresh liquid-Zn could flow into the crack through the convection/capillarity phenomena and crack opening becomes self-boosted. In this manner, the local propagation path of the crack is governed by the austenite HABs; however, the overall crack propagation path is controlled by the direction of the applied tensile stress. As mentioned, by the accumulation of Zn along austenite HABs and exceeding the maximum Zn-solubility in austenite (7 wt%), α-Fe(Zn) start to form locally at the crack opening area as a result of the Zn strong ferrite stabilizing effect. The diffusivity of Zn in γ-Fe and α-Fe at 850 °C is 1.11×10^{-17} and 3.53×10^{-15} m^2/s, respectively [26]. Therefore, the formation of α-Fe along the LME-crack promotes Zn penetration due to the higher diffusion distance of Zn. In accordance with the previous reports [26,27,36], the formation of α-Fe(Zn) in Zn-penetrated regions at high temperatures adjacent to austenite could assist the loss of ductility as the ferrite is a soft phase. Finally, during the cooling cycle, austenite transforms into a lath martensitic structure; however, α-Fe(Zn) fine grains adjacent to the LME-crack remain stable due to high Zn content (stage IV).

The research works by Ashby and Easterling and Ion et al. [39–41] showed that Rosenthal's solution for a fast moving power source on a thin plate can effectively predict microstructural evolution such as grain growth and martensite development within the HAZ. Further investigations by Xia et al. [42] also confirmed that by employing experimental measurements from the weld cross-sections, the Rosenthal model can successfully calculate the hold times at temperatures of interest within HAZ during LBW of various AHSS grades. According to this model for prediction of microstructural evolution within HAZ, hold times at the temperature range during LBW of steels could be determined by the Eq. (2):

$$\tau = \frac{1}{4\pi e \lambda \rho c} \frac{\left[\frac{Q_{net}}{vd}\right]^2}{\left(T_{Ac_3} - T_0\right)^2} \tag{2}$$

where ρ is the steel density (7870 kg/m^3), c is the steel specific heat capacity (420 J/kg/K), λ is the thermal conductivity (39 W/m/K) [43], T_0 is the ambient temperature, Q_{net} is the laser power, v is welding speed, d is

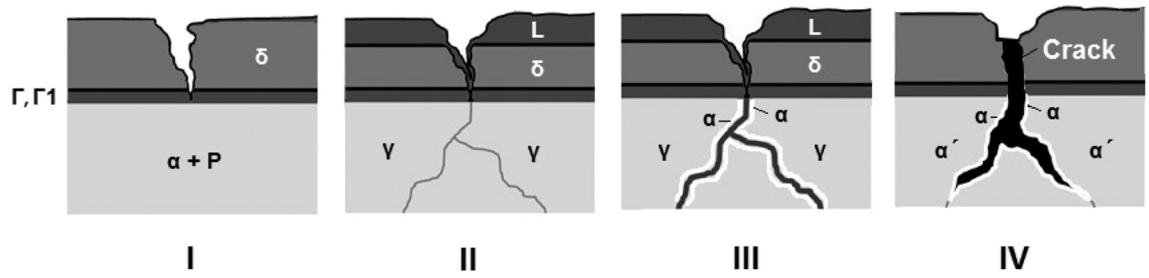

Fig. 11. The schematic of LME mechanism during FLW of GA-coated 22MnB5 steel (α: Ferrite, P: Pearlite, γ: Austenite, α′: Martensite, δ: Fe-Zn delta-phase, L: Liquid, Γ/Γ1: Gamma/Gamma1).

sheet thickness, and $\frac{Q_{net}}{vd}$ is so-called heat-input and known as the thickness normalized net absorbed energy per unit weld length. Microstructural evaluations (Fig. 8) confirmed the occurrence of LME-cracking within the UCHAZ, hence, in the present work T_{Ac_3} has been into consideration. Through substitution of direct experimental measurements of r_{Ac_3} and r_m isotherm positions of T_{Ac_3} and T_m (melting point) from the different weld cross-sections, heat input is calculated accordingly:

$$\frac{Q_{net}}{vd} = \frac{\rho c\left(r_{Ac_3} - r_m\right)(2\pi e)^{1/2}}{\left(\frac{1}{T_{Ac_3} - T_0} - \frac{1}{T_m - T_0}\right)} \tag{3}$$

After heat input calculations, time constant revealing the time at the critical temperature range within HAZ would be determined. Fig. 12 presents the time constant in different experimental welding conditions. As is seen, time constant varies between 2 and 8 ms in different welding conditions in the present work; whereas higher heat-inputs results in higher time constants. Increasing the LME-crack length with increasing time constant is in agreement with diffusion-based penetration of Zn along the austenite HABs during the welding cycle. The concurrency of heat, tensile stress, and liquid metal above certain limits can result in the occurrence of LME [11]. Therefore, it is logical to expect an increased probability of LME with increasing heat-input and subsequently hold time at the upper-critical zone. Higher heat input could result in more coating melting, a higher kinetics of Zn-diffusion along the austenite HABs and ferritic transformation. This justifies increased LME susceptibility with increasing heat-input (time constant) (Fig. 12). This agrees with previous studies on the effect of a higher heat-input in the promotion of LME during other welding methods such as RSW [5,6].

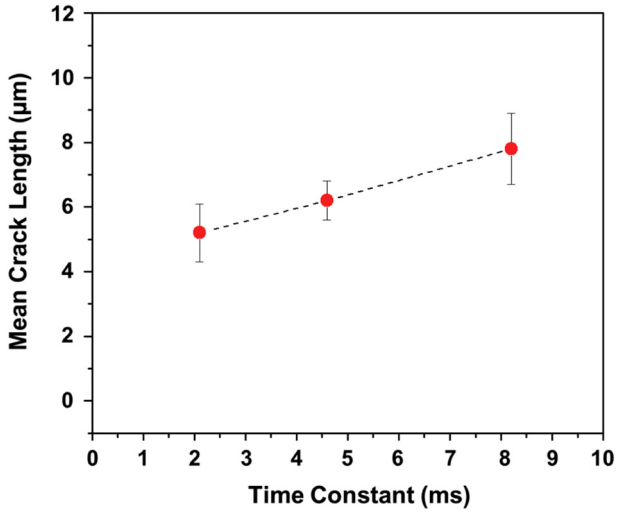

Fig. 12. Mean crack length vs. time constant in different welding conditions (under constant normalized tensile stress of 100% of YS).

4. Conclusions

The present work developed a new method to study barely reported LME phenomenon during LBW of Zn-coated 22MnB5 PHS. The following conclusions could be drawn:

(a) The results indicated that there exists a direct correlation between the applied external load and LME susceptibility. The threshold tensile stress of about 80%YS is necessary to trigger LME during LBW of the material. Accordingly, LME microcracking takes place between 80 and 110% YS; however, under a tensile stress of 115% YS, LME-cracks with an average length of about 70 μm appeared within the upper-critical heat-affected zone. Applied stress level over 120% YS ends in rapid crack propagation into the FZ and an abrupt rupture during the welding.

(b) Partial melting of the Fe-Zn δ and Γ/Γ1 phases within the coating and flowing through the pre-existing coating-cracks resulted in penetration of Zn along austenite HABs. The penetration of Zn along austenite HABs led to intergranular decohesion of the material. Due to the rapid crack opening, more liquid-Zn could flow into the crack by the capillarity phenomenon.

(c) The accumulation of Zn along the HABs over the maximum solubility in the austenite, promotes α-Fe(Zn) formation. The formation of α-Fe(Zn) along Zn-penetration area assist the loss of ductility due to the higher Zn diffusivity in α-Fe. The diffusion-based penetration of Zn along austenite HAGs was also confirmed by means of the Rosenthal model.

(d) Based on the above and considering that the risk temperature range of 700–1000 °C and low exposure times could easily come across within UCHAZ, to control the embrittlement in the GA-coated steel and achieve reliable LME-free laser welds, external tensile stress during the process should be kept <80% of YS. The LME cracking could also be alleviated by lower heat inputs during LBW.

Acknowledgements

Authors would like to acknowledge the National Science and Engineering Research Council (NSERC) of Canada, International Zinc Association, in Durham, USA, and ArcelorMittal Dofasco Inc. in Hamilton, Canada for providing the financial support and materials to carry out this work.

References

[1] M. Rajagopalan, M.A. Bhatia, M.A. Tschopp, D.J. Srolovitz, K.N. Solanki, Atomic-scale analysis of liquid-gallium embrittlement of aluminum grain boundaries, Acta Mater. 73 (2014) 312–325.

[2] M. Naderi, M. Peterlechner, E. Schafler, S.V. Divinski, G. Wilde, Kinetic, volumetric and structural effects induced by liquid Ga penetration into ultrafine grained Al, Acta Mater. 99 (2015) 196–205.
[3] B. Joseph, M. Picat, F. Barbier, Liquid metal embrittlement: a state-of-the-art appraisal, Eur. Phys. J. Appl. Phys. 5 (1999) 19–31.
[4] I. Serre, J. Vogt, Mechanical properties of a 316L/T91 weld joint tested in lead – bismuth liquid, Mater. Des. 30 (2009) 3776–3783.
[5] R. Ashiri, M. Shamanian, H.R. Salimijazi, M.A. Haque, J.H. Bae, C.W. Ji, K.G. Chin, Y. Do Park, Liquid metal embrittlement-free welds of Zn-coated twinning induced plasticity steels, Scr. Mater. 114 (2016) 41–47.
[6] R. Ashiri, M. Shamanian, H.R. Salimijazi, M.A. Haque, C.W. Ji, Y. Do Park, Supercritical area and critical nugget diameter for liquid metal embrittlement of Zn-coated twinning induced plasticity steels, Scr. Mater. 112 (2016) 156.
[7] D. Favez, L. Deillon, J. Wagnie, M. Rappaz, Intergranular penetration of liquid gold into stainless steel, Acta Mater. 59 (2011) 6530–6537.
[8] R.C. Hugo, R.G. Hoagland, The kinetics of gallium penetration into aluminum grain boundaries-in situ TEM observations and atomistic models, Acta Mater. 48 (2000) 1949–1957.
[9] E. Perreiro-Lopez, W. Ludwig, D. Bellet, C. Lemaignan, In situ investigation of Al bicrystal embrittlement by liquid Ga using synchrotron imaging, Acta Mater. 54 (2006) 4307–4316.
[10] E. Perreiro-Lopez, W. Ludwig, D. Bellet, Discontinuous penetration of liquid Ga into grain boundaries of Al polycrystals pez, Acta Mater. 52 (2004) 321–332.
[11] H. Nam, D.J. Srolovitz, Effect of material properties on liquid metal embrittlement in the Al – Ga system, Acta Mater. 57 (2009) 1546–1553.
[12] W. Ludwig, D. Bellet, In situ investigation of liquid Ga penetration in Al bicrystal grain boundaries: grain boundary wetting or liquid metal embrittlement? Acta Mater. 53 (2005) 151–162.
[13] B. Joseph, F. Barbier, M. Aucouturier, Grain boundary penetration of liquid Bi in Cu polycrystals, Mater. Sci. Forum, Trans Tech Publ 1999, pp. 735–738.
[14] C. Beal, X. Kleber, D. Fabregue, M. Bouzekri, Embrittlement of a zinc coated high manganese TWIP steel, Mater. Sci. Eng. A 543 (2012) 76–83.
[15] C. Beal, X. Kleber, M. Bouzekri, Liquid zinc embrittlement of twinning-induced plasticity steel, Scr. Mater. 66 (2012) 1030–1033.
[16] A. Hojna, F. Di Gabriele, On the kinetics of LME for the ferritic – martensitic steel T91 immersed in liquid PbBi eutectic, J. Nucl. Mater. 413 (2011) 21–29.
[17] X. Gong, P. Marmy, L. Qin, B. Verlinden, M. Wevers, M. Seefeldt, Effect of liquid metal embrittlement on low cycle fatigue properties and fatigue crack propagation behavior of a modified 9Cr – 1Mo ferritic – martensitic steel in an oxygen-controlled lead – bismuth eutectic environment at 350 C, Mater. Sci. Eng. A 618 (2014) 406–415.
[18] J. Zhou, B. Wang, M. Huang, Two constitutive descriptions of boron steel 22MnB5 at high temperature, J. Mater. 63 (2014) 738–748.
[19] M. Nikravesh, M. Naderi, G.H. Akbari, W. Bleck, Phase transformations in a simulated hot stamping process of the boron bearing steel, Mater. Des. 84 (2015) 18–24.
[20] J. Kaars, P. Mayr, K. Koppe, Generalized dynamic transition resistance in spot welding of aluminized 22MnB5, Mater. Des. 106 (2016) 139–145.
[21] Z. Xiang Gui, W. Kang Liang, Y. Liu, Y. Sheng Zhang, Thermo-mechanical behavior of the Al-Si alloy coated hot stamping boron steel, Mater. Des. 60 (2014) 26–33.
[22] M. Abbasi, M. Naderi, A. Saeed-Akbari, Isothermal versus non-isothermal hot compression process: a comparative study on phase transformations and structure-property relationships, Mater. Des. 45 (2013) 1–5.
[23] H. Karbasian, A.E. Tekkaya, A review on hot stamping, J. Mater. Process. Technol. 210 (2010) 2103–2118.
[24] M.H. Razmpoosh, A. Macwan, E. Biro, Y. Zhou, Effect of coating weight on fiber laser welding of Galvanneal-coated 22MnB5 press hardening steel, Surf. Coat. Technol. 337 (2018) 536–543.
[25] X. Wang, X. Chen, Q. Sun, H. Di, L. Sun, Formation mechanism of delta-ferrite and metallurgy reaction in molten pool during press-hardened steel laser welding, Mater. Lett. 206 (2017) 143–145.
[26] H. Kang, L. Cho, C. Lee, B.C. De Cooman, Zn penetration in liquid metal embrittled TWIP steel, Metall. Mater. Trans. A. 47 (2016) 2885–2905.
[27] C.W. Lee, W.S. Choi, L. Cho, Y.R. Cho, B.C. De Cooman, Liquid-metal-induced embrittlement related microcrack propagation on Zn-coated press hardening steel, ISIJ Int. 55 (2015) 264–271.
[28] T. Böllinghaus, H. Herold, C.E. Cross, J.C. Lippold, Hot Cracking Phenomena in Welds II, Springer Science & Business Media, 2008.
[29] GM4485M, Weld Specification For Lasers Welds - Butt Joints, 2002 1–6.
[30] A.R. Marder, Metallurgy of zinc-coated steel, Prog. Mater. Sci. 45 (2000) 191–271.
[31] B. Hutchinson, J. Hagstro, Microstructures and hardness of as-quenched martensites (0.1–0.5%C), Acta Mater. 59 (2011) 5845–5858.
[32] A. Bardelcik, C.P. Salisbury, S. Winkler, M.A. Wells, M.J. Worswick, Effect of cooling rate on the high strain rate properties of boron steel, Int. J. Impact Eng. 37 (2010) 694–702.
[33] M. Isakov, T. Nyysso, Iterative determination of the orientation relationship between austenite and martensite from a large amount of grain pair misorientations, Metall. Mater. Trans. A 47 (2016) 2587–2590.
[34] L. Ryde, Application of EBSD to analysis of microstructures in commercial steels, Mater. Sci. Technol. 22 (2006) 1297–1306.
[35] H. Järvinen, M. Isakov, T. Nyyssönen, M. Järvenpää, P. Peura, The effect of initial microstructure on the final properties of press hardened 22MnB5 steels, Mater. Sci. Eng. A 676 (2016) 109–120.
[36] L. Cho, H. Kang, C. Lee, B.C. De Cooman, Microstructure of liquid metal embrittlement cracks on Zn-coated 22MnB5 press-hardened steel, Scr. Mater. 90 (2014) 25–28.
[37] N. Haghdadi, A. Zarei-Hanzaki, E. Farabi, P. Cizek, H. Beladi, P.D. Hodgson, Strain rate dependence of ferrite dynamic restoration mechanism in a duplex low-density steel, Mater. Des. 132 (2017) 360–366.
[38] P.N.P. Pokorny, J. Kolisko, L. Balik, Description of structure of Fe-Zn intermetalic compounds present in hot-dip galvanized coatings on steel, Meta 54 (2015) 707–710.
[39] E. Biro, J.R. McDermid, J.D. Embury, Y. Zhou, Softening kinetics in the subcritical heat-affected zone of dual-phase steel welds, Metall. Mater. Trans. A. 41 (2010) 2348–2356.
[40] M.F. Ashby, K.E. Easterling, A first report on diagrams for grain growth in welds, Acta Metall. 30 (1982) 1969–1978.
[41] J.C. Ion, K.E. Easterling, M.F. Ashby, A second report on diagrams of microstructure and hardness for heat-affected zones in welds, Acta Metall. 32 (1984) 1949–1962.
[42] M. Xia, E. Biro, Z. Tian, Y.N. Zhou, Effects of heat input and martensite on HAZ softening in laser, ISIJ Int. 48 (2008) 809–814.
[43] B.T. Tang, S. Bruschi, A. Ghiotti, P.F. Bariani, Numerical modelling of the tailored tempering process applied to 22MnB5 sheets, Finite Elem. Anal. Des. 81 (2014) 69–81.